PAPER

CrossMark
← click for updates

Tuning the Cu$_x$O nanorod composition for efficient visible light induced photocatalysis†‡

Pradip Basnet* and Yiping Zhao

A facile, low cost, and convenient method to fabricate Cu$_x$O (x = 1, 2) nanorod (NR) arrays is demonstrated by thermally oxidizing Cu NRs fabricated by oblique angle deposition. The single phase Cu$_2$O and CuO, and mixed phase Cu$_2$O/CuO polycrystalline NRs can be tuned simply by varying the thermal oxidation temperature. These Cu$_x$O NRs exhibit excellent visible light photocatalytic activity for both cationic (methylene blue) and anionic (methyl orange) dye degradations. When used as a photocathode, they also show good photoelectrochemical performance, especially the mixed phase Cu$_2$O/CuO NRs. The maximum stable photocurrent density is observed to be 0.24 mA cm^{-2} under a simulated solar light. Incident photon-to-current efficiencies are found to be 20% and 44% at incident light wavelengths λ = 500 nm and 400 nm, respectively. These results show that the Cu$_x$O NRs fabricated through the oxidation method can be a suitable candidate for efficient visible light active photocatalysts for energy applications as well as for wastewater treatment.

Department of Physics and Astronomy, and Nanoscale Science and Engineering Center, University of Georgia, Athens, Georgia 30602, USA.
E-mail: pbasnet@physast.uga.edu; Fax: (706) 542 2492; Tel: (706) 542 6230
† The authors declare no competing financial interest.
‡ Electronic supplementary information (ESI) available: (1) Transmittance (%T') and reflectance (%R) spectra of Cu$_x$O NRs, (2) Tauc's plot for direct and indirect bandgap calculations, (3) self-degradation of MB and MO dyes under visible light illumination, (4) estimation of pseudo-first order dye degradation rates, (5) H$_2$O$_2$ assisted photocatalytic activity, (6) decolorization/mineralization tests towards oxidation, and (7) stability tests for Cu$_x$O NR samples. See DOI: 10.1039/c5cy01464f

Introduction

Visible light active photocatalysts (VLAPCs) have recently attracted tremendous attention for their renewable energy and environmental applications, such as wastewater treatment and bacterial inhibition.[1–4] Unlike traditional large bandgap photocatalysts, such as titania (TiO$_2$), zinc oxide (ZnO), and tungsten oxide (WO$_3$) nanostructures, VLAPCs better utilize available solar irradiation ($\lambda \geq$ 400 nm) for more efficient catalytic activity.[2,3,5] There are two general ways to generate efficient VLAPCs: either by modifying well known photocatalysts such that they absorb visible light by doping or constructing heterostructures,[6,7] or by exploring the photocatalytic properties of new materials with small energy band gaps, such as CuO, Cu$_2$O, α-Fe$_2$O$_3$, CoO, Bi$_2$O$_3$, BiVO$_4$, etc.[8–12] Among these small bandgap materials, copper oxides (Cu$_x$O; x = 1, 2) hold great potential due to their unique optical and charge transport properties.[11,13–15] Cu$_2$O and CuO, both p-type semiconductors, are suitable for visible light

absorption because of their favorable bandgap values that range from 1.7 to 2.6 eV.[13,16] Cu$_2$O is considered more attractive for photocatalysis since its conduction band lies just above the water reduction potential (0 V vs. NHE), and its bandgap is about 2.0–2.2 eV, which is larger than the water oxidation potential, 1.23 eV, but remains in the visible region.[8] In addition to photocatalysis, Cu$_2$O and CuO nanostructures have been studied for solar energy conversion,[9] antimicrobial applications,[10] gas sensing,[17] and lithium-ion batteries.[14,18] The use of a Cu$_2$O nanostructure as a photocathode is also promising due to its favorable energy band positions, with the conduction band (CB) lying more negative than the H$_2$ evolution potential and the valance band (VB) lying just positive of the O$_2$ evolution potential.[1,19] However, there are a limited number of reports describing the photoelectrochemical (PEC) properties of Cu$_x$O nanostructures, and those that do exist indicate that the stability of Cu$_x$O nanostructures could be a potential problem for light related applications. This is because the redox potential for Cu$_2$O reduction exists within its bandgap, and theoretically Cu$_2$O can be reduced to Cu by photoexcited electrons, which causes photoreduction/corrosion.[1] Thus, there are several conflicting reports appearing in the literature. For example, Yu et al. studied CuO/Cu$_2$O microspheres for methyl orange (MO) degradation under visible light irradiation and reported that no significant photocatalytic degradation was achieved unless aided by H$_2$O$_2$ as a hole scavenger.[16] On the other hand, Zhou et al.[20] and Chen et al.[18] separately reported excellent photocatalytic activity of Cu$_2$O/Cu nanocomposites and Cu/Cu$_2$O core–shell nanowires for dye degradations of MO and

methylene blue (MB). Hara *et al.* has reported on a lengthy water splitting test on Cu_2O powders under solar irradiation and observed no noticeable activity loss for 1900 hours.[9] Later de Jongh *et al.* published a paper questioning the stability of the Cu_2O nanostructure for PEC water splitting *via* normal photocatalytic reaction.[21] Since then, several other papers have been published showing differing results on the photocatalytic stability of Cu_2O.[19,22–24] In addition, Paracchino *et al.* and Zhang *et al.* have independently studied the stability of Cu_2O with and without the protecting layers of $Al/ZnO/TiO_2$ and CuO.[1,24] Their results have shown that the photocatalytic stability of Cu_2O nanostructures with coatings was enhanced. Interestingly, Zhang *et al.* has interpreted the enhanced stability due to the crystallographic orientation of Cu_2O along the [111] plane.[24] The exact reason for these conflicting observations is not clear yet. Recently, Bendavid and Carter suggested that the stability of Cu_2O nanostructures is closely related to their crystallographic orientations,[25] which implies that the Cu_xO fabrication technique may play a dominant role.

Both wet chemical methods, such as electrodeposition,[22,23] hydrothermal synthesis,[26] and sol–gel,[27] and vapor-phase based methods, such as thermal oxidation,[28,29] sputtering,[30] microwave irradiation,[31] direct oxidation in air,[32] and physical vapor deposition (PVD),[28] have been reported to prepare Cu_xO nanostructures. Among these techniques, PVD is a versatile, reliable, low cost, and fast deposition technique for the fabrication of thin films and nanostructures. In particular, PVD is advantageous based on the fact that one can control the porosity of nanostructured thin films when the system is arranged into an oblique angle deposition (OAD) configuration.[4,28,33] OAD is a simple and well-known technique in which the incident material vapor is directed toward a substrate at large incident angles (>70°) with respect to the substrate surface normal, resulting in self-organized, aligned, and tilted nanorod (NR) arrays.[4,34] The growth of NRs is controlled by the geometric shadowing effect and surface diffusion of vapor adatoms. Detailed descriptions of the growth process can be found in some recent review articles.[35] Our previous works have proven that OAD is a versatile method in fabricating efficient polycrystalline photocatalyst NRs.[4,7,34,36,37] It is expected that aligned and polycrystalline Cu_xO NR arrays would have different photocatalytic activities if their crystalline phase and compositional properties could be changed and tuned, and the relative stability problem could also evolve with the crystal phases.

In this report, a facile fabrication method of Cu_xO NRs based on OAD is demonstrated. The sample preparation strategy is to first deposit the Cu NRs using the OAD technique, then to oxidize the as-prepared Cu NRs under ambient conditions for a predetermined time at a given temperature. Depending on the oxidation temperature, one can obtain the single phase Cu_2O and CuO, or the mixed phase Cu_2O/CuO NRs. The visible light induced photocatalytic activities of these Cu_xO NRs are investigated for degradations of both the

cationic (MB) and anionic (MO) dyes. In addition, with the help of a small amount of H_2O_2, a significant increase in the degradation rates is observed for both the MB and MO dyes. The PEC properties and stability of the Cu_xO NR samples are strongly dependent on applied bias potentials. All the nanostructures are stable for the photodecay test, but in PEC measurements under visible light illumination and at a negative bias potential, the photocurrents from all the samples degrade with illumination time. The CuO NR sample is relatively more stable than the other two samples, while the Cu_2O NR sample is the least stable.

Results and discussion

Morphology and structural properties

Fig. 1(a) shows the representative top and cross-sectional view SEM images of as-deposited Cu NR samples. Morphology related parameters such as the direction of vapor incident angle θ, NR tilting angle β, NR vertical thickness h, and NR diameter D are also defined in Fig. 1(a). Fig. 1(a) reveals that the as-prepared Cu nanostructure consists of well-aligned and tilted NRs. From the top-view SEM image, the NR density η is estimated to be $\eta = 50 \pm 10$ rods per μm^2. These NRs are straight and exhibit a relatively smooth side surface, which is consistent with the result reported by Li *et al.*[28] The cross-sectional image in Fig. 1(a) shows that the Cu NRs are nearly cylindrical in shape with increasing diameter towards the top. The average width (or diameter) of the NRs near the top is $D = 40 \pm 10$ nm. To make a fair comparison, we measured the diameters of both the Cu and Cu_xO
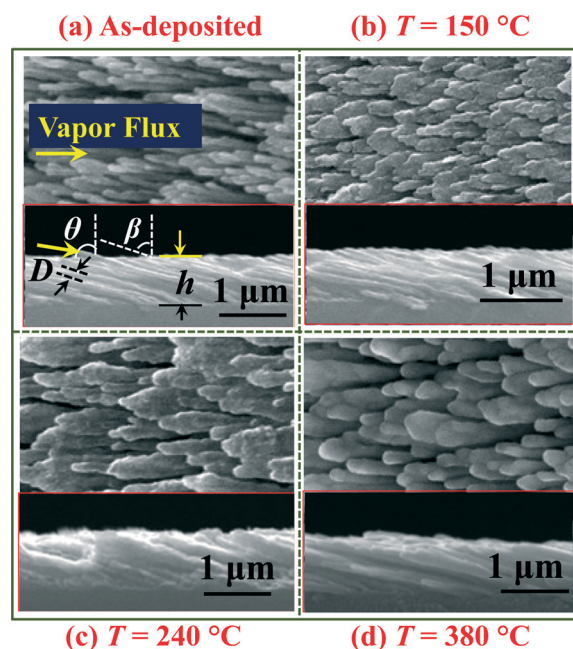

Fig. 1 Top-view SEM images of (a) as-deposited Cu NRs, (b) Cu_2O NRs, oxidized at $T = 150$ °C, (c) Cu_2O/CuO NRs, oxidized at $T = 240$ °C, and (d) CuO NRs, oxidized at $T = 380$ °C. Figure insets represent their respective cross-sectional views.

NRs at about 100 nm below the top surface. These Cu NRs are tilting away from the substrate normal at $\beta = 70 \pm 5°$ and $h = 350 \pm 20$ nm. The measured value of β does not match the angle predicted by both the tangent rule,[38] $\beta = \arctan(1/2 \tan\theta) = 82°$; and the cosine rule,[39] $\beta = \theta - \arcsin((1 - \cos\theta)/2) = 58°$, for OAD. However, the material dependent models described in the literature can be used to explain the resulting β angle.[40] Fig. 1(b) to (d) show the representative SEM images of Cu_xO NR samples obtained at oxidation temperatures $T = 150, 240,$ and 380 °C, respectively. Compared to Fig. 1(a), the changes in the morphology of Cu_xO NR samples are obvious; visually one can see that the NR diameter becomes larger after oxidation, which is expected. Other morphological parameters such as h, β, and η are also changed, and the results are summarized in Table 1. The increase in diameter could be interpreted as oxidation and coarsening of NRs with increasing oxidation temperature. As a result, the NR density is found to be decreased with T. Regardless of the oxidation temperatures, the β values are observed to be almost unchanged.

The crystal structures of Cu_xO NRs are characterized by XRD. Fig. 2(a) shows the XRD patterns of Cu_xO NR samples oxidized at different temperatures. The XRD pattern of the as-deposited Cu NRs (Fig. 2(a)) is also included as a reference, and the result shows that these samples are polycrystalline Cu with no detectable impurities (as compared with JCPDS ref. no. 085-1326). All the diffraction peaks of the sample oxidized at $T = 150$ °C, namely at $2\theta = 29.58°, 36.44°, 42.33°, 61.41°,$ and $73.56°$, are consistent with the diffraction patterns of Cu_2O (JCPDS ref. no. 078-2076), representing the Cu_2O crystal planes of (110), (111), (200), (220), and (311), respectively. While the sample oxidized at $T = 380$ °C is composed of pure single phase CuO (JCPDS no. 048-1548) as confirmed by the peaks at $2\theta = 32.51°, 35.42°, 35.54°, 38.71°, 38.90°, 48.72°, 53.49°, 58.26°, 61.53°, 65.81°, 66.22°, 67.90°, 68.12°, 72.37°, 74.98°,$ and $75.24°$, which represent the (110), (002), (11$\bar{1}$), (111), (200), (20$\bar{2}$), (020), (202), (11$\bar{3}$), (022), (31$\bar{1}$), (113), (220), (311), (004) and (22$\bar{2}$) crystal planes of CuO. Nevertheless, all the samples oxidized in the temperature range, 150 °C < T < 380 °C, have a mixture of Cu_2O and CuO phases, which is consistent with the thin film results reported in the literature.[15,16]

The phase evolution and nanocrystal growth of Cu_2O and CuO NRs can be further understood through detailed XRD
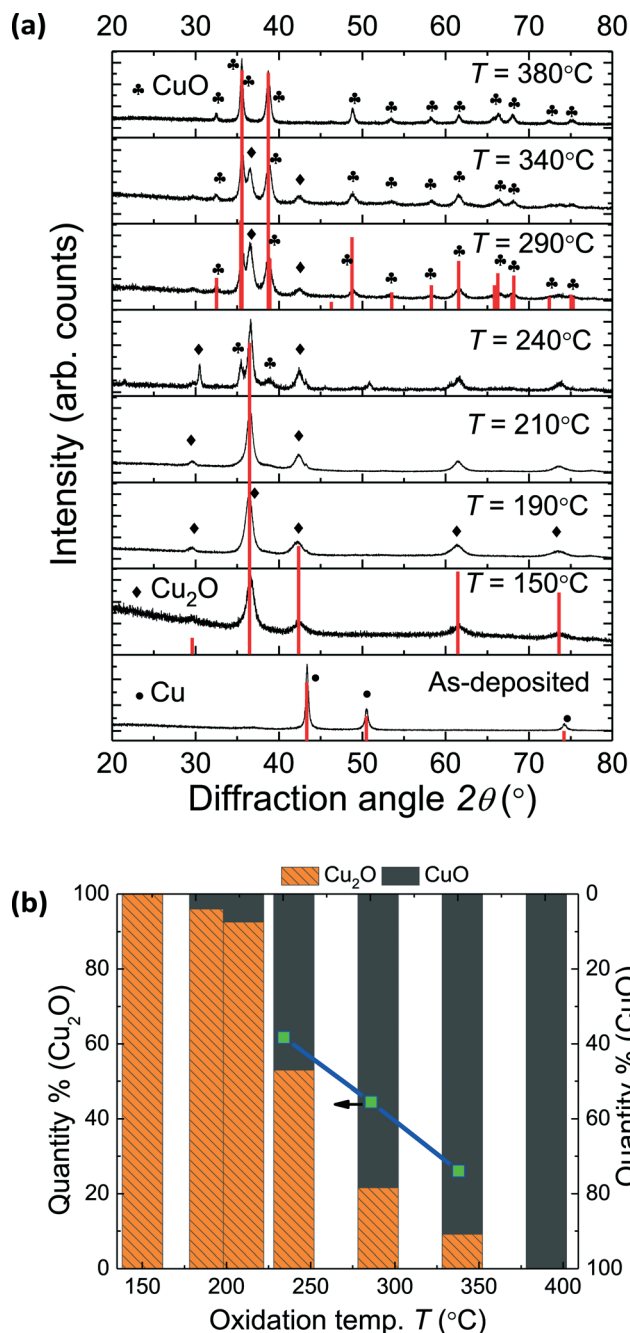

Fig. 2 (a) Comparison of XRD patterns of as-deposited Cu and oxidized Cu_xO NR samples, and (b) the change of the Cu_2O to CuO composition ratio in the Cu_xO NR samples, estimated through XRD patterns, as a function of oxidation temperature T.

Table 1 Summary of SEM image analysis for the morphology of Cu and Cu_xO NRs

	As-deposited Cu	$T = 150$ °C Cu_2O	$T = 240$ °C Cu_xO (mixed)	$T = 380$ °C CuO
NR tilting angle, β (°)	70 ± 5	70 ± 5	70 ± 5	74 ± 5
NR thickness, h (nm)	350 ± 20	340 ± 20	340 ± 20	320 ± 20
Density, η (# per μm^2)	50 ± 10	45 ± 10	45 ± 10	40 ± 10
NR diameter, D (nm)	40 ± 10	50 ± 10	60 ± 10	70 ± 10

analysis. First, the average crystallite sizes can be estimated using the most prominent peaks of the Cu_2O (111), CuO (111), and CuO (11$\bar{1}$) planes by the Scherrer equation, $d = K\lambda / \beta' \cos\theta$, where d is the diameter of the crystalline grain, $K = 0.9$, λ (Cu-Kα_1) = 1.5405980 Å, and β' is the full width at half maximum (FWHM) of the selected diffraction peak. Note that for the accurate estimation of the real crystallite size of each samples one needs to know the line broadening due to the XRD instrument and the lattice strain/disorder using a

standard reference material. According to Suryanarayana, one can use the raw XRD data to compare the trend of change in crystallite size as we are interested in the relative structural changes for different oxidation temperatures.[41] Results of the estimated crystallite sizes are summarized in Table 2. Overall, the estimated crystallite sizes of Cu_2O and CuO increase with T (with the exception of the samples annealed at $T = 290$ °C and 340 °C). This deviation could be attributed to the peak broadening due to the phase change from Cu_2O to CuO, i.e., changing the XRD peak position from $2\theta = 36.44°$ of Cu_2O to 35.42° and 35.54° of CuO (see Fig. 2(a)). Besides, the general trend of increasing the estimated crystallite size of CuO at higher T is in good agreement with the observed NR coarsening.[18] In addition, the XRD data can also be used to roughly estimate the Cu_2O/CuO composition ratio through a semi-quantitative analysis utilizing the Rietveld program using the FullProf software as described in the literature.[42,43] The use of the Rietveld procedure (whole profile) can be considered as a reliable method to estimate the weight percentage (wt%) of each component in the mixture. Fig. 2(b) shows the relative wt% of Cu_2O and CuO for different oxidation temperatures. The Cu_2O wt% in the Cu_xO NR samples oxidized at $T =$ 150, 190, 210, 240, 290, 340, and 380 °C is estimated to be 100%, 96%, 92.5%, 53%, 21.6%, 9.2%, and 0%, respectively. These results can also be confirmed by using ratios of the most prominent peaks of Cu_2O (111) and CuO (111), as described in the literature.[16] The estimated results are shown by a blue line in Fig. 2(b). The increased amount of CuO with oxidation temperature is reasonable since more and more Cu_2O is oxidized into the more stable CuO phase at higher T. It is also expected that such an oxidation process starts from the outer surface of the Cu_2O NRs and progresses inwards.

Optical properties

The appearance of an as-deposited Cu NR sample and some representative oxidized Cu_xO NR samples are shown in the inserts of Fig. 3(a). The Cu NR sample is optically opaque and highly reflective by visual inspection. After oxidation, the Cu_xO NR samples appear to be pale yellowish in color at lower T (≤ 240 °C) and then change slowly into darker reddish black with increasing T (240 °C $\geq T \leq 380$ °C). This
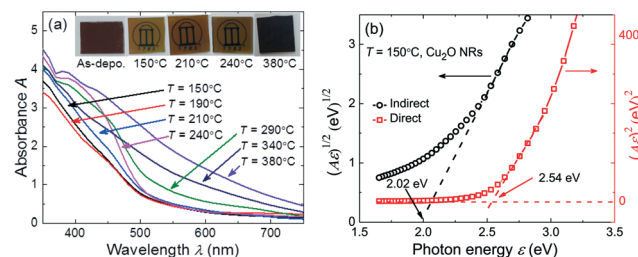

Fig. 3 (a) Absorption spectra of Cu_xO NR samples and (b) the representative Tauc's plot showing a direct and an indirect bandgap for the Cu_2O NR sample. Insets in (a) show the digital photographs of Cu_xO samples oxidized at different T values, placed over the University of Georgia logo.

shows that the visible light absorption of the sample is increased at higher T values. The optical absorbance spectra (A) of the Cu_xO NR samples are obtained by measuring both the transmittance (%T') and reflectance (%R) spectra,

$$A = \alpha \cdot h = \ln\left(\frac{1-R}{T'}\right), \qquad (1)$$

where α and h are the absorption coefficient and thickness of the film, respectively. Representative transmittance and reflectance spectra of the Cu_xO NR samples are shown in Fig. S1 in the ESI,‡ and the estimated UV-vis absorbance spectra of these samples are shown in Fig. 3(a). The absorption edges of the oxidized samples are red-shifted with increasing T (with the exception of the sample oxidized at $T = 190$ °C). This general trend can be attributed to the crystal phase change, as confirmed by the XRD results. The optical bandgaps of these Cu_xO NR samples are estimated using Tauc's plots with the following relationship,

$$A\varepsilon = A_0(\varepsilon - E_g)^m, \qquad (2)$$

where ε is the photon energy, A_0 is a constant relative to the material, and m is an exponent indicating a direct bandgap material ($m = 1/2$) and an indirect bandgap material ($m = 2$).[4,14] As reported in the literature, Cu_xO could exhibit both direct and indirect band gap behaviors.[14,15] Therefore, Tauc's plots are obtained for both the direct and indirect allowed transitions. Fig. 3(b) shows an example of the Tauc's plots for the Cu_2O NR sample at $T = 150$ °C. The direct and indirect bandgaps of Cu_2O NRs are determined to be $E_g^D = 2.54$ and $E_g^I = 2.02$ eV, respectively. The Tauc's plots for all other Cu_xO NR samples are shown in Fig. S2(a) and (b) in the ESI;‡ and the resulting bandgap values are summarized in Table 2. Results show that the single phase Cu_2O and the mixed phase Cu_2O/CuO samples exhibit both direct and indirect bandgaps while the single phase CuO NR samples only exhibit a direct transition (see Fig. S2(b) in the ESI‡). The direct bandgap of the single phase CuO NRs is 2.13 eV. Similar phenomena for the Cu_2O and CuO films have been reported by Heinemann et al. and Zoolfakar et al.[14,15] The estimated direct bandgap values of Cu_2O NRs ($E_g^D = 2.54$ eV) are in good agreement

Table 2 Structural and optical parameters of Cu_xO NR samples

Sample	Structural parameters		Optical parameters	
	Estimated grain size (nm) at (111), Cu_2O phase	Estimated grain size (nm) at (111)/(1$\bar{1}$1), CuO phase	Direct bandgap	Indirect bandgap
$T = 150$ °C	6.4	—	2.54	2.02
$T = 190$ °C	7.7	—	2.51	2.04
$T = 210$ °C	8.5	—	2.50	2.06
$T = 240$ °C	9.2	—	2.50	1.94
$T = 290$ °C	—	12.8/7.6	2.45	2.16
$T = 340$ °C	—	17.0/10.4	2.24	—
$T = 380$ °C	—	19.9/14.3	2.13	—

with the results reported for Cu_2O thin films which are in the range of $E_g = 2.1–2.6$ eV.[12,15,29] However, the estimated values for indirect bandgaps of our Cu_2O NR samples are slightly lower than those reported in the literature (2.1–2.21 eV).[14,15] These observed lower values could be due to various reasons, such as heat treatment (during oxidation), change or restriction in grain sizes during crystal phase change, composition of mixed phases, *etc.*, as reported by Zoolfakar *et al.*[14]

Photocatalytic activity

The photocatalytic dye degradations (PDD) of both the MB and MO aqueous solutions are tested to characterize the catalytic activity of Cu_xO NR samples under visible light irradiation. The reason for choosing MB and MO dyes is that they are the two most popular dyes for photocatalytic activity tests, and one (MB) is cationic and one (MO) is anionic.[44,45] Different Cu_xO NR samples could exhibit different uptake capacities *via* dark adsorption. Two control experiments are performed. The first experiment is to monitor the dark adsorption of dyes onto the Cu_xO NRs by keeping the dyes in the dark with Cu_xO samples for 30 to 60 min. No significant dark adsorption of both the dyes is observed with all the Cu_xO NR samples. The second experiment is to investigate the direct photodecay of the dyes by irradiating the dye solutions with light without the Cu_xO samples. We observed a slow decrease in the absorption spectra of MB solution but no obvious change for MO solution (see Fig. S3(a) and (b) in the ESI‡). The decay rate constant for MB is estimated to be $k_{light}^{MB} = 0.003 \pm 0.001$ h^{-1}. This result suggests that there is a self-degradation of MB under visible light irradiation. The plots of MB and MO absorption peak *versus* illumination time are shown in Fig. S4(a) and (b) in the ESI,‡ and the decay constant κ_c value extracted from these plots as a function of Cu_2O weight percentage γ is plotted in Fig. 4. Note that γ decreases monotonically with T. We observe two trends: first, the photodecay rates κ_c for both MB and MO follow the same trend with respect to γ (or T); second, the MB degradation rates are relatively higher than those of the MO degradation rates. It is clear that under the same testing conditions, the single phase CuO NR samples

give the lowest photocatalytic performance for both the cationic and anionic dyes while the single phase Cu_2O NR samples show relatively high κ_c. Such a difference can be explained by the amount of reactive oxygen species (ROS) produced on the surface of a photocatalyst.[46] The generation of ROS is strongly dependent on the amount of photogenerated CB electrons and VB holes, and more importantly on the redox potentials of a photocatalyst (see Fig. 5(a) and (b)). The higher ROS generation rate can be expected if the CB edge is more negative and the VB edge is more positive (see Fig. 5(b)). Thus, the low degradation rate with the single phase CuO NR sample compared to that of the single phase Cu_2O NR sample could be due to its CB edge lying in a position unfavorable for multiple electron transfer (see Fig. 5(b)).[22] For the CuO sample, its CB edge is approximately located at +0.0 to 0.03 V (V *vs.* NHE) while the required O_2 reduction potential is −0.28 V as shown in Fig. 5(b).[47] Therefore, the CB location could not provide a sufficient potential to reduce the molecular O_2 through electron transfer, $O_{2(ads)} + e^- \rightarrow O_2^-$.[48,49] But its VB edge is more positive than the H_2O oxidation potential (+1.23 eV), which can generate a hydroxyl radical, $OH_{(ads)}^- + h^+ \rightarrow OH_{(ads)}^·$, leading to the generation of hydrogen peroxide, $2OH^· \rightarrow H_2O_2$. Overall, this results in a low efficiency in generating ROS. In contrast, the single phase Cu_2O samples have a more negative CB edge, reported to be located at −1.2 to −1.4 V (V *vs.* NHE), and its VB edge is located around +1.1 to +1.3 V (V *vs.* NHE) (deduced from the bandgap), which is potentially for a higher ROS generation rate.[47,49]

When T increases from 150 °C to 210 °C, the γ changes slightly, from 100% to 92.5%, and the photodecay rate also decreases slightly by considering the error bar in the measurements. This is due to the phase transition of Cu_2O to CuO. When T reaches 240 °C, γ becomes 53% and κ_c increases from ~0.06–0.07 h^{-1} to ~0.084 h^{-1}. Such an increase in κ_c could be due to the competition of the reduced amount of Cu_2O and the increased Cu_2O/CuO interface. By changing Cu_2O to CuO, the photodecay rate κ_c is expected to decrease as discussed above. However, since part of Cu_2O is converted into CuO, there will be an increased amount of Cu_2O/CuO interfaces formed. Due to the different bandgap and CB/VB locations of Cu_2O and CuO, a heterostructure is formed at these interfaces,
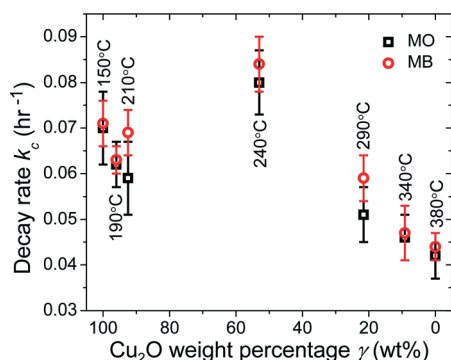

Fig. 4 Photocatalytic decay rates κ_c as a function of Cu_2O weight percentage γ, obtained at different T values, for MO and MB degradations under visible light illumination.
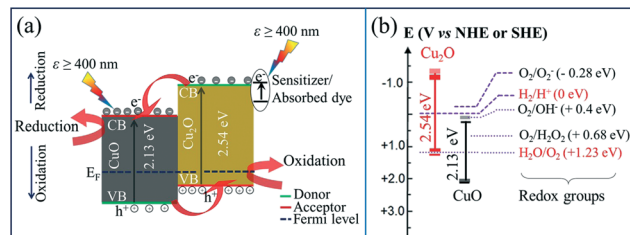

Fig. 5 The proposed mechanism for the enhancement of the photocatalytic activity for MB and MO with the mixed phase Cu_2O/CuO NR samples. (a) Generation and transfer of charge carriers. Note that the electron and hole transfer directions for Cu_2O/CuO composites are shown by red arrows. (b) Energy band edges of single phase Cu_2O and CuO NRs with redox couples in water.

which could take advantage of the energy band misalignment of both the Cu_2O and CuO. As shown in Fig. 5(a), at the Cu_2O/CuO interface, a charge separation process could occur: the CB electrons of higher energy from Cu_2O can move to the CB of CuO (lower energy) while the VB holes from CuO could transfer to the VB of Cu_2O (energetically favorable). In these processes, the Cu_2O sample acts as an electron donor and hole acceptor while the opposite applies for the CuO sample. Charge separation at the interface of the mixed phase Cu_2O/CuO samples is very advantageous in extending the lifetime of photogenerated electron–hole pairs, to avoid their recombination, which may result in an enhanced PDD activity.[5,50] Similar mechanisms have been described in the literature for heterojunction of metal oxide semiconductors.[16,18,37] Our experimental observation infers that when T increased from 150 °C to 240 °C, the effect of hetero-interface or charge separation will surpass the effect caused by the phase transition from Cu_2O to CuO, and give a net increase in κ_c when T increased to 240 °C. However, when T increases further (>240 °C), more Cu_2O changes to CuO, and the amount of Cu_2O/CuO interfaces should decrease eventually, thus less charge separation is expected, which results in lower κ_c. In the meantime, more Cu_2O is changed into CuO, which also induced further reduction in κ_c. Both effects result in a faster loss in κ_c values after $T > 240$ °C and bring about the almost linear decrease in κ_c with respect to γ as shown in Fig. 4.

In order to explain the difference in decay rates of MB and MO, we need to consider the role of dyes in photodecay characterization. According to the literature, the overall photocatalytic activity observed is governed by two pathways, the direct semiconductor photoexcitation and indirect dye photosensitization.[51] The latter process of photosensitization (also called photo-assisted degradation) involves a two-step process: excitation of the dye *via* visible light absorption and transfer/injection of excited electron(s) onto the CB of a photocatalyst as shown in Fig. 5(a).[52] In overall photocatalytic process, the amount of light absorbed by the individual dye is used to determine the indirect photosensitization, which contributes to the total decay rate. It is expected that under the same experimental conditions, the more light absorbed by a dye, the higher the photodecay rate. Therefore, we compare the absorbance spectra of the dye solutions, the Cu_xO NR samples, and the emission spectrum of the light source used for the photocatalytic experiments. As seen in Fig. 6, the MB absorbs the light in the wavelength range of 550 to 700 nm (λ_{max} at 664 nm) while MO absorbs light from 380 to 530 nm (λ_{max} at 465 nm). MB has a larger absorption band and the source light covers the entire MB absorption spectra. As a consequence, more photoexcited electrons are expected to be injected into the CB of a photocatalyst resulting in a higher MB degradation rate. As described above, the self-degradation of the MB solution may also contribute to the higher decay rates.

To confirm the stability of the Cu_xO NR samples in PDD reactions, MB and MO degradation experiments are repeated for three successive cycles for each of the Cu_xO sample. Then
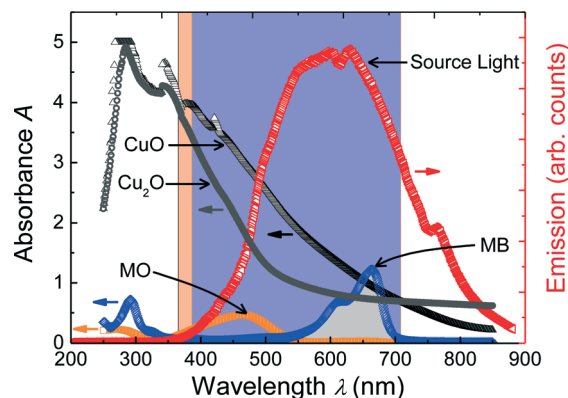

Fig. 6 The comparison of the absorbance spectra of Cu_xO NR samples, and dye absorbance spectra (MO & MB) as well as the emission spectrum of illuminating light.

the XRD patterns, UV-vis transmittance, and decay rates after each test and with reference to the fresh sample are used to compare their stability. Fig. S8 in the ESI‡ shows the representative results of MB degradation with the Cu_2O NR sample, used for a total of 21 h of experiments. The photocatalytic activities are observed to remain about the same (less than 5% change in the total degradation), indicating that the prepared Cu_2O NR samples are stable in aqueous solution and under visible light irradiation. Similarly, other Cu_xO NR samples also retained their photocatalytic activity after multiple experiments. Fig. S9 and S10 in the ESI‡ show a representative XRD patterns and the UV-vis transmittance spectra of some selected Cu_xO NR samples, respectively, *i.e.* before and after the dye degradation experiments. No changes in the crystal structures and optical absorbance are observed under the detection limit of instruments, indicating that these Cu_xO NR samples are fairly stable during the photocatalytic reaction in aqueous solution. These results could be attributed to the dominated crystallographic orientation of Cu_2O, *i.e.* along the [111] plane as confirmed by the XRD (see Fig. 2(a)).[22,25] While the stability for mixed phase Cu_2O/CuO and the single phase CuO samples are in good agreement with the literature, single phase CuO is reported to be the most stable and it also improves the stability of Cu_2O by acting as a protecting layer.[22,24]

Furthermore, in order to make a fair comparison of the dye degradation efficiency of our best sample (Cu_2O/CuO NRs, $T = 240$ °C) with the literature we used the optimized amount of H_2O_2, *i.e.*, 0.01 : 3 H_2O_2 to dye volume ratio (v/v) suggested in the literature,[53] and tested the photodecay performance for both MB and MO solutions. Significant enhancements have been observed in the degradation rates for both dyes, resulting in 90% and more decolorization of both MO and MB in 7 h (see Fig. S5(a)–(d) and S6(a)–(d) in the ESI‡). These enhancements are about 5.4 and 3.7 times higher compared to the decay rates of MB and MO without the use of H_2O_2 (see Fig. S5(d) and S6(d) in the ESI‡), and these values are much higher than the reported value for MO degradation (~14% removal of MO in 5 h) with a mixed phase

Cu_2O/CuO hollow microsphere.[16] It is important to note that in ref. 16, the authors have used 0.2 g of Cu_2O/CuO powder in 20 ml of MO aqueous solution similar to the initial concentration (31 μM) we used, but the light intensity is relatively low (0.46 mW cm^{-2}).

We further tested the final dye solutions obtained from these experiments to indirectly confirm the permanent composition change (see Fig. S7(a)–(d) in the ESI‡). Purging the solutions with oxygen (~10 sccm) for 30 min did not reversibly change the dye color back, *i.e.* at least for 2 h. So, we believe that the photocatalytic reaction mechanisms are dominated by complete mineralization, but not by forming the leuco-MB and protonated MO *via* charge transfer.[54,55] The observed results that are best fitted with the Langmuir–Hinshelwood kinetic model further validated the above conclusion regardless of the use of H_2O_2.[50,55]

Photoelectrochemical (PEC) properties

The cyclic voltammetry (CV), dynamic photoresponse, and incident photon-to-current efficiency (IPCE) measurements are performed to characterize the PEC properties of Cu_xO NR samples.[1] Three representative samples, namely, a single phase Cu_2O NR sample ($T = 150$ °C), a mixed phase Cu_2O/CuO NR sample ($T = 240$ °C), and a single phase CuO NR sample ($T = 380$ °C), are characterized. Multi-cycle CV measurements are used to determine the redox potentials and the stability of these samples in the electrolyte solution. Some of the selected cyclic voltammograms are shown in Fig. 7(a) to (c). Three different scanning rates, 100 mV s^{-1}, 50 mV s^{-1}, and 10 mV s^{-1}, are chosen to confirm if any oxidative and reductive peaks are missing at the highest scan rate. Unless otherwise stated, here we show the cyclic voltammogram results from −0.6 to + 0.6 V obtained from a scan rate of 100 mV s^{-1}. As seen in Fig. 7(a) to (c), over the entire potential range, both the cathodic and anodic peaks are observed for all three samples. The single phase Cu_2O and the mixed phase Cu_2O/CuO NR samples are observed to be relatively unstable for the first few minutes (Fig. 7(a) & (b)), but these stabilized in about 10 minutes, while the CuO NR sample is observed to be the most stable one (see Fig. 7(c)). The cathodic and anodic peaks for the Cu_2O NR sample are observed at potentials $V_c = -0.16$ V, $V_c = -0.42$ V, and $V_a = +0.52$ V, which are consistent with the reported characteristic reduction and oxidation peaks of Cu_2O and CuO.[22] For the mixed phase Cu_2O/CuO NR sample, with the increased number of cycles, initially the observed $V_a = +0.25$ V moves towards more positive values as shown in Fig. 7(b) while the $V_a = +0.01$ V almost disappeared. The CV of the CuO NR sample exhibits only one cathodic ($V_c = -0.39$ V) and one anodic ($V_a = +0.25$ V) peaks (Fig. 7(c)). The observed variations in the voltammograms, for different samples, demonstrate that the stability of Cu_xO NRs are strongly phase dependent where the CuO NR sample exhibit the most stable phase. These results are in good agreement with the report by Zhang *et al.*, who have reported an enhanced stability of Cu_2O nanostructures

by coating a protecting thin layer of CuO.[24] For the Cu_2O NR sample, the maximum stable cathodic and anodic current density values are observed to be $J_c = 0.38$ mA cm^{-2} and $J_a = 0.85$ mA cm^{-2}, respectively. Further, it is observed that the cathodic current density decreases beyond $V_c = -0.16$ V until it reaches another plateau at $V_c = -0.42$ V where the cathodic current stabilized to $J_c = 0.31$ mA cm^{-2}. For the mixed phase Cu_2O/CuO sample, the maximum cathodic and anodic current densities are $J_c = 0.82$ mA cm^{-2} and $J_a = 1.2$ mA cm^{-2}, respectively. Beyond the cathodic peak, $V_c = -0.36$ V, for $V \leq -0.5$ V, J_c is observed to increase almost linearly with the applied potential. The maximum stable cathodic and anodic current densities for the single phase CuO NR sample are $J_c = 0.5$ mA cm^{-2} and $J_a = 0.35$ mA cm^{-2}. The J_c–V_c also shows a linear relationship for $V \leq -0.5$ V. This linear behavior for the both single phase Cu_2O and mixed phase Cu_2O/CuO samples could be attributed to the increased reduction while the absence in
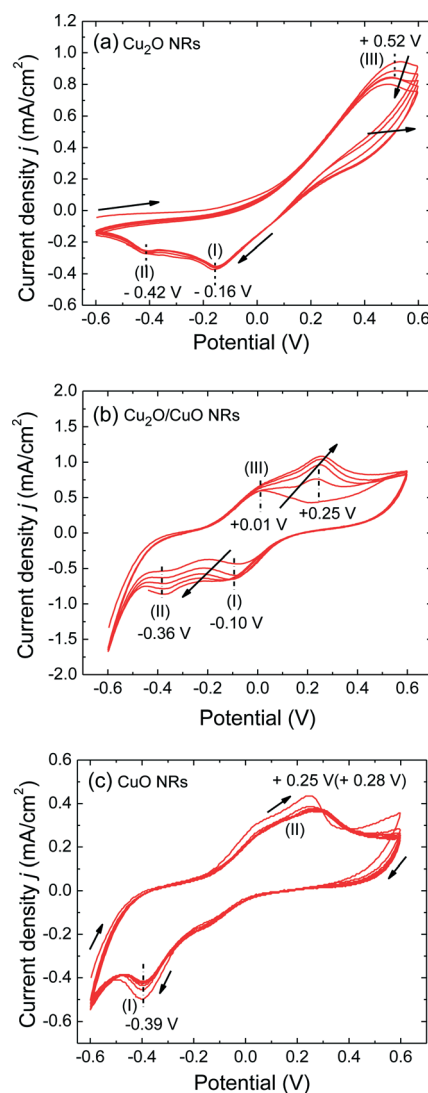

Fig. 7 The CV curves of selected Cu_xO NR samples: (a) Cu_2O ($T = 150$ °C), 5 cycles; (b) Cu_2O/CuO ($T = 240$ °C), 5 cycles; and (c) CuO ($T = 380$ °C), 10 cycles.

the Cu_2O NR sample could be due to the diffusion control current.[56]

Fig. 8(a) shows the dynamic photocurrent generation curves, the photocurrent density J_{ph} versus time t, for the three samples tested in 0.5 M Na_2SO_4 at a bias potential of $V_c = -0.5$ V and under the illumination of AM1.5G. The chopping frequency is 0.033 Hz. The observed photo-induced cathodic currents demonstrate the p-type semiconductor nature of these samples.[23,56] For all the three samples the J_{ph}–t curves show that the initial J_{ph} values are large and then decrease with chopping times, which is consistent with the results from most of the PEC
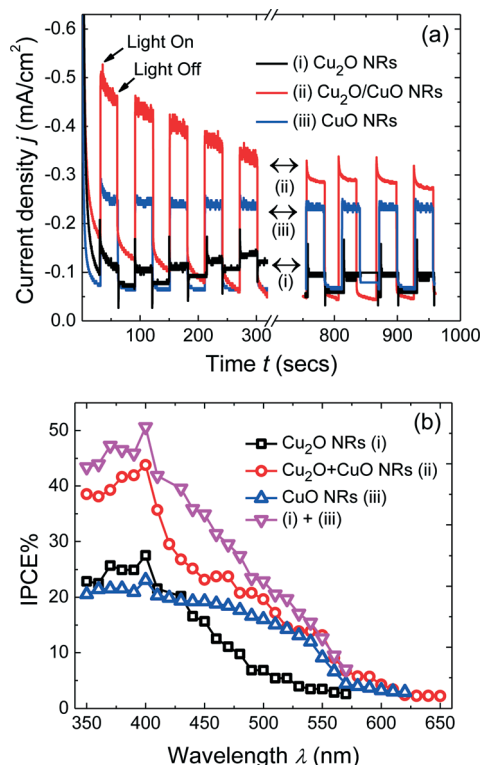

measurements. Note that the J_{ph} decreases for the single phase Cu_2O sample and the mixed phase Cu_2O/CuO sample relatively quickly, while for the single phase CuO sample, J_{ph} decreases much slower (see Fig. S11 in the ESI‡). After 15 minutes, we observed about 15% loss in the photocurrent for Cu_2O, about 33% for mixed phase Cu_2O/CuO, and only 2% for the CuO NR sample. The single phase Cu_2O sample shows the lowest stable $J_{ph} = 0.06$ mA cm^{-2} while the Cu_2O/CuO sample demonstrates the highest J_{ph} (0.24 mA cm^{-2}). The CuO sample has moderate $J_{ph} = 0.18$ mA cm^{-2}. This result is consistent with the observed PDD results, discussed in the previous section, except for the single phase CuO and Cu_2O samples. The main reason for the mixed Cu_2O/CuO sample to have the maximum J_{ph} could be due to the charge separation effect at the Cu_2O/CuO interface, as explained above. The applied negative bias to the single phase CuO sample causes its CB to move towards a more negative location, resulting in enhanced J_{ph} values. A similar argument can be applied to the single phase Cu_2O sample where a more negative CB location far beyond the O_2 reduction potential results in a low reaction efficiency, hence a lower photoresponse.[27,57]

The IPCE spectra for the three samples are shown in Fig. 8(b) for the bias $V_c = -0.5$ V. As expected, the overall higher IPCE% is observed for the mixed phase Cu_2O/CuO NR sample: the highest IPCE% value is estimated to be 44% at $\lambda = 400$ nm and it decreases monotonically with an increase in wavelength. At $\lambda = 550$ nm, the IPCE is still about 10% which indicates that most of the visible photons have been successfully converted into photocurrents. The IPCE values for Cu_2O and CuO NR samples are observed almost the same and remain as a constant (20–27%) in a wavelength regime of $\lambda \leq 430$ nm. The Cu_2O NR sample exhibits a slightly higher efficiency (e.g. at $\lambda = 400$ nm, 27% for Cu_2O and 23% for CuO). However, when $\lambda > 400$ nm, the IPCE for Cu_2O decreases quickly from 27% to 7% at $\lambda = 500$ nm, while for CuO, it decreases very slowly from 23% at $\lambda = 400$ nm to 16% at $\lambda = 500$ nm. This explains why the J_{ph} of the CuO sample is larger than that of Cu_2O samples. By closely examining the IPCE spectra of the three samples, we notice that the IPCE response of the Cu_2O/CuO sample almost overlaps with that of the CuO

Fig. 8 (a) Photocurrent response and (b) IPCE spectra of selected Cu_xO NR samples (cathode) in 0.5 M Na_2SO_4 solution under solar simulator (1 sun) at −0.5 V vs. Ag/AgCl.

Table 3 Summary of PEC performances for H_2 evolution and/or photocurrrent generation of some of the visible light active photocatalysts

Photocatalyst	Electrolyte, potential bias, and light source	STH% and/or J_{ph} (mA cm^{-2})	IPCE value at 400 nm	Ref. year
Cu_2O/CuO nanorods	0.5 M Na_2SO_4, −0.5 V vs. Ag/AgCl, AM1.5G	0.24 mA cm^{-2}	44%	Our work
α-Fe_2O_3 nanostructures, with and without (Co–Pi)[a]	Un-buffered NaOH aq. solution (pH 13.6), 1.23 V vs. RHE, AM1.5G	~0.24 mA cm^{-2} for α-Fe_2O_3 and 0.435 mA cm^{-2} with Co-Pi co-catalyst	—	59 2015
CoO nanoparticles	Neutral water, no bias, AM1.5G	~5% STH	—	60 2014
β-Bi_2O_3 thin film	0.5 M Na_2SO_3, AM1.5	0.45 mA cm^{-2} at 1.23 V vs. NHE	43% at 0.197 V vs. NHE	61 2013
$BiVO_4$ (Co–Pi catalyzed)	0.5 M K_2SO_4 (buffered to pH ~5.6 with 0.09 M KH_2PO_4/0.01 M K_2HPO_4), 1.23 V vs. RHE, AM1.5	1.7 mA cm^{-2}	>80% between 340 and 420 nm at low light intensities (few μW cm^{-2})	62 2012
Co-Pi/$BiVO_4$/WO_3	0.5 M Na_2SO_4, 1.23 V vs. RHE, AM1.5	3.2 mA cm^{-2}	60%	63 2014

[a] Co–Pi (cobalt phosphate).

samples when $\lambda > 500$ nm, while for $\lambda < 400$ nm, Cu_2O/CuO and Cu_2O samples have similar spectral shapes. In Fig. 8(b) we also plot the sum of the IPCE spectra of single phase CuO and Cu_2O and compare it with that of mixed phase Cu_2O/CuO. Besides the difference in the magnitude for $\lambda < 550$ nm, the spectral shapes are very similar. Clearly the mixed phase Cu_2O/CuO sample greatly enhances the PEC efficiency. Overall, the PEC performance of our Cu_2O/CuO NR ($T = 240$ °C) sample is promising based on the fact that it can be easily fabricated from pure metallic Cu, and the composition can be tuned relatively easily. However, the photocurrent density of the best Cu_2O/CuO NR sample is still low when compared to the composite or heterostructured VLAPs reported in the literature, as summarized in Table 3. For more comprehensive details about the single and dual absorber materials including their benchmark values we refer the reader to review papers by Paracchino et al., Moniz et al., and Ager et al.[1,48,58]

Conclusions

In summary, we have synthesized the single phase Cu_2O and CuO, and the mixed phase Cu_2O/CuO NR samples with different mass ratios of Cu_2O/CuO by a simple OAD and post-deposition oxidation method. The single phase Cu_2O NRs have both the direct ($E_g = 2.54$ eV) and indirect ($E_g = 2.02$ eV) electronic transitions while the single phase CuO samples only exhibit a direct transition ($E_g = 2.13$ eV). All of the Cu_xO samples are active and efficient in PDD and PEC under visible light irradiation. A significant enhancement in PDD is observed when aiding the optimal amount of H_2O_2. We have also found that all Cu_xO NR samples are stable in PDD reactions while for the PEC performance the single phase CuO NR sample is relatively more stable compared to both the single phase Cu_2O sample and mixed phase Cu_2O/CuO sample. Among the three samples, the mixed phase Cu_2O/CuO sample shows the best PEC performance, with photocurrent $J_{ph} = -0.24$ mA cm^{-2} under AM1.5G, and broad spectra response, with IPCE = 44% at $\lambda = 400$ and 10% at $\lambda = 550$ nm. Further investigations need to be conducted to reduce or eliminate the degradation effect of the mixed phase Cu_2O/CuO sample in order to achieve a much better performance for photocatalysis and PEC applications.

Experimental section

Materials

Copper shot (99.9+%) and titanium pellets (99.995%) were purchased from Alfa Aesar (Ward Hill, MA) and Kurt J. Lesker (Clairton, PA). Cleaned glass microscope slides (Gold Seal® catalog no. 3010), indium tin oxide (ITO) coated glass slides ($R_s = 8$–12 Ω; Delta Tech. Ltd.) and Si (100) wafers (Montco Silicon Technologies Inc.) were used as substrates for material deposition. High purity methylene blue (MB, $C_{16}H_{18}ClN_3S$; CAS #122965-43-9) and methyl orange (MO, $C_{14}H_{14}N_3NaO_3S$; CAS #547-58-0) were obtained from Alfa Aesar (Ward Hill, MA). Hydrogen peroxide (H_2O_2, 30% H325-500) solution was

purchased from Fisher Scientific (Pittsburgh, PA). Sodium sulfate, anhydrous (Na_2SO_4), was purchased from J.T. Baker Chemicals (BAKER ANALYZED, A.C.S. Reagent, 3898-01).

Sample preparation

Both the Ti adhesion layer and Cu NR arrays were deposited onto the substrates by a custom designed vacuum deposition system equipped with an electron-beam evaporation source (Torr International, Inc.). The glass, ITO, and Si substrates were cut into sizes of 9.0 mm × 27.0 mm, 15 mm × 10 mm, and 10.0 mm × 10.0 mm, respectively. Glass substrates were cleaned by a piranha solution using a 4 : 1 mixture of sulphuric acid (H_2SO_4) and hydrogen peroxide (H_2O_2) solution. Si wafers and ITO substrates were cleaned using a 5 : 1 : 1 mixture of deionized (DI) water, H_2O_2, and aqueous ammonia (NH_4OH) solution. Both the glass substrates and the Si wafers were boiled in their respective solutions for 15 minutes before being dried under nitrogen flow. Prior to the deposition, the chamber was evacuated to a base pressure of less than 1×10^{-6} Torr. During the deposition, the pressure was maintained to about $\leq 3 \times 10^{-5}$ Torr. A 20 nm thick Ti adhesion layer was deposited at the vapour incident angle $\theta = 0°$ with respect to the substrate normal. Then the Cu NRs were deposited at $\theta = 86°$. The deposition rate and thickness were monitored by a quartz crystal microbalance (QCM) positioned directly facing the vapor flux. For both Ti and Cu depositions, the deposition rates were maintained at 0.4 nm s^{-1}. For Cu NR arrays, the final QCM thickness reading was 2 μm.

The as-deposited Cu NR samples were then oxidized in a quartz tube furnace (Lindberg/Blue M Company) at preset temperatures of 150, 190, 210, 240, 290, 340 and 380 °C, respectively, under ambient conditions or under oxygen (O_2) flow (20 sccm) to obtain different phases of Cu_xO NRs. During all the treatments, the temperature was ramped at a rate of 5 °C min^{-1} and the samples were maintained at the final temperature for 3 hours.

Characterization

The morphology and composition of the Cu and Cu_xO NR samples were examined by using a field-emission scanning electron microscope (SEM) equipped with an energy dispersive X-ray spectroscope (FEI Inspect F). The crystal structure of the samples were characterized by using a PANalytical X'Pert PRO MRD X-ray diffractometer (XRD) with a fixed incidence angle of 0.5°. The XRD patterns were recorded with Cu Kα$_1$ radiation ($\lambda = 1.5405980$ Å) in the 2θ range from 20 to 80° at a step size of 0.010°. XRD patterns were used to determine the crystal phase(s), their average crystallite size(s) and the relative wt% of Cu_2O/CuO of the samples oxidized at different temperatures. The optical transmittance of the samples was measured by using a double beam UV-visible light (UV-vis) spectrophotometer (JASCO V-570) over a wavelength range from 350 to 850 nm. While the reflectance of the samples were measured at normal incidence using a monochromator and a calibrated beam splitter (THORLABS Inc. Model:

50/50 BSW26), and baseline correction was done with a silver mirror (THORLABS Inc. Model: PF10-03-P01) using a home-built spectrometer system.

Photocatalytic activities of the Cu_xO NR samples were evaluated by the degradations of MB and MO aqueous solutions under visible light irradiation at room temperature (25 ± 2 °C). Note that the detailed photodecay processes of MB and MO are complicated since different reaction products could be produced, leading to conversion of sulfur and nitrogen heteroatoms to sulfate, nitrate, and ammonium ions.[50,55,64] A more thorough assessment of the real photocatalytic performance shall require the measurements of the composition of each product as a function of the decay time, and the use of the mineralized product of the dye to assess the ultimate photodecay rate.[50,53] This would be a very tedious process and require advanced instruments. Here we still adapt the general photodecay characterization method used in most of the literature since the main purpose is to characterize the photodecay performance of materials with a similar structure and composition. The starting concentrations of the dyes were chosen to be 31.3 μM for MB and 30.5 μM for MO, and their respective pH values were 6.4 (± 0.2) and 5.7 (± 0.2). The Cu_xO NR samples were placed into a 10 mm × 10 mm × 45 mm clear methacrylate cuvette filled with 3.0 ml of the dye solution. Prior to light irradiation, each sample in the dye solution remained in the dark for 30–60 min in order for the dye molecules to reach adsorption/desorption equilibrium on NRs. The cuvette was then illuminated by using a 250 W quartz halogen lamp (UtiliTech) covering a wavelength range from 390 to 850 nm. The illumination area on the samples was fixed at 2.43 cm^2 at a constant light intensity of 65 mW cm^{-2}, as monitored by using an optical power meter equipped with a thermal sensor (Thorlabs PM100D/S310C). A water filter was placed in front of the cuvette to absorb the IR light. The photodegradation kinetics of the MB and MO were measured by examining their time dependent characteristic optical absorption peaks, at $\lambda = 664$ nm for MB and $\lambda = 465$ nm for MO.[4,33] The time dependent absorption data were fitted by a pseudo-first order decay equation, $\alpha(t) = \alpha(0)e^{-\kappa_c t}$, where $\alpha(0)$ is the initial absorbance at time $t = 0$ min, in order to obtain the decay constant κ_c.

PEC measurements were performed in a home-made single compartment cell with a quartz window (%$T' > 90\%$ in the visible wavelength range) and conventional 3-electrode arrangement using a potentiostat (Pine Instrument AFCBP1 Bipotentiostat). The Cu_xO NR samples deposited on ITO substrates were placed inside the PEC cell, with the deposited NRs facing directly towards the illuminating light through the quartz window. The exposure areas were 1 cm × 1 cm and were used as the working electrodes (WE). An Ag/AgCl electrode (3 M KCl) was used as a reference (RE), and a platinum (Pt) coil (diameter ~0.5 cm and length ~5 cm) was used as a counter electrode (CE). The electrolyte, 0.5 M sodium sulfate (Na_2SO_4) solution, was aerated with N_2 for an hour; the initial pH value of the electrolyte was 6.9 ± 0.2. The CV of the samples was measured in the dark at room temperature

(25 ± 2 °C), while the photoresponse and IPCE measurements were performed with a solar simulator (AM1.5G, Oriel Instruments, USA, Newport Corp. Model# 69911) and a monochromatic light source (APEX, Newport Corp. Model: 74100). The illumination area of the monochromator beam, onto the Cu_xO NR samples, was 0.6 cm × 0.4 cm while the area of the collimated beam from the solar simulator was 1 cm × 1 cm. The incident intensity of the solar simulator, at the quartz window of the PEC cell, was adjusted to be 100 mW cm^{-2} (1 sun equivalent). And the IPCE measurements were performed from 350 nm to 750 nm at every 10 nm interval. The resolution of the monochromatic source light was adjusted to 2.5 nm. All the PEC measurements were performed under a bias potential of −0.5 V (vs. Ag/AgCl). Note that the value of bias potentials, V (vs. Ag/AgCl), is not the same as the reversible hydrogen electrode (RHE) or normal hydrogen electrode (NHE) potentials, but they can be converted according to V(RHE or NHE) = V + 0.197 V + pH (0.059 V).[27] Therefore, all the potential values listed above are V versus Ag/AgCl, unless otherwise stated.

Acknowledgements

Notes and references

1 A. Paracchino, V. Laporte, K. Sivula, M. Grätzel and E. Thimsen, Nat. Mater., 2011, 10, 456–461.
2 A. Kudo and Y. Miseki, Chem. Soc. Rev., 2009, 38, 253–278.
3 Z.-G. Zhao and M. Miyauchi, Angew. Chem., Int. Ed., 2008, 47, 7051–7055.
4 P. Basnet, G. K. Larsen, R. P. Jadeja, Y.-C. Hung and Y. Zhao, ACS Appl. Mater. Interfaces, 2013, 5, 2085–2095.
5 L. Wang, J. Ge, A. Wang, M. Deng, X. Wang, S. Bai, R. Li, J. Jiang, Q. Zhang, Y. Luo and Y. Xiong, Angew. Chem., Int. Ed., 2014, 53, 5107–5111.
6 N. Feng, Q. Wang, A. Zheng, Z. Zhang, J. Fan, S.-B. Liu, J.-P. Amoureux and F. Deng, J. Am. Chem. Soc., 2013, 135, 1607–1616.
7 W. Smith and Y. P. Zhao, J. Phys. Chem. C, 2008, 112, 19635–19641.
8 X. Chen, C. Li, M. Grätzel, R. Kostecki and S. S. Mao, Chem. Soc. Rev., 2012, 41, 7909–7937.
9 M. Hara, T. Kondo, M. Komoda, S. Ikeda, J. N. Kondo, K. Domen, M. Hara, K. Shinohara and A. Tanaka, Chem. Commun., 1998, 357–358.
10 G. Ren, D. Hu, E. W. C. Cheng, M. A. Vargas-Reus, P. Reip and R. P. Allaker, Int. J. Antimicrob. Agents, 2009, 33, 587–590.

11 J. C. Park, J. Kim, H. Kwon and H. Song, *Adv. Mater.*, 2009, **21**, 803–807.

12 B. K. Meyer, A. Polity, D. Reppin, M. Becker, P. Hering, P. J. Klar, T. Sander, C. Reindl, J. Benz, M. Eickhoff, C. Heiliger, M. Heinemann, J. Bläsing, A. Krost, S. Shokovets, C. Müller and C. Ronning, *Phys. Status Solidi B*, 2012, **249**, 1487–1509.

13 M. Yin, C.-K. Wu, Y. Lou, C. Burda, J. T. Koberstein, Y. Zhu and S. O'Brien, *J. Am. Chem. Soc.*, 2005, **127**, 9506–9511.

14 A. S. Zoolfakar, R. A. Rani, A. J. Morfa, A. P. O'Mullane and K. Kalantar-zadeh, *J. Mater. Chem. C*, 2014, **2**, 5247–5270.

15 M. Heinemann, B. Eifert and C. Heiliger, *Phys. Rev. B: Condens. Matter Mater. Phys.*, 2013, **87**, 115111.

16 H. Yu, J. Yu, S. Liu and S. Mann, *Chem. Mater.*, 2007, **19**, 4327–4334.

17 J. Zhang, J. Liu, Q. Peng, X. Wang and Y. Li, *Chem. Mater.*, 2006, **18**, 867–871.

18 W. Chen, Z. Fan and Z. Lai, *J. Mater. Chem. A*, 2013, **1**, 13862–13868.

19 P. E. de Jongh, D. Vanmaekelbergh and J. J. Kelly, *J. Electrochem. Soc.*, 2000, **147**, 486–489.

20 B. Zhou, Z. Liu, H. Wang, Y. Yang and W. Su, *Catal. Lett.*, 2009, **132**, 75–80.

21 P. E. de Jongh, D. Vanmaekelbergh and J. J. Kelly, *Chem. Commun.*, 1999, 1069–1070.

22 L. Wu, L.-K. Tsui, N. Swami and G. Zangari, *J. Phys. Chem. C*, 2010, **114**, 11551–11556.

23 S. Emin, F. F. Abdi, M. Fanetti, W. Peng, W. Smith, K. Sivula, B. Dam and M. Valant, *J. Electroanal. Chem.*, 2014, **717–718**, 243–249.

24 Z. Zhang and P. Wang, *J. Mater. Chem.*, 2012, **22**, 2456–2464.

25 L. I. Bendavid and E. A. Carter, *J. Phys. Chem. B*, 2013, **117**, 15750–15760.

26 X. P. Gao, J. L. Bao, G. L. Pan, H. Y. Zhu, P. X. Huang, F. Wu and D. Y. Song, *J. Phys. Chem. B*, 2004, **108**, 5547–5551.

27 Y.-F. Lim, C. S. Chua, C. J. J. Lee and D. Chi, *Phys. Chem. Chem. Phys.*, 2014, **16**, 25928–25934.

28 H. F. Li, A. K. Kar, T. Parker, G. C. Wang and T. M. Lu, *Nanotechnology*, 2008, **19**, 335708.

29 V. Figueiredo, E. Elangovan, G. Goncalves, P. Barquinha, L. Pereira, N. Franco, E. Alves, R. Martins and E. Fortunato, *Appl. Surf. Sci.*, 2008, **254**, 3949–3954.

30 J. Deuermeier, J. Gassmann, J. Brötz and A. Klein, *J. Appl. Phys.*, 2011, **109**, 113704.

31 D. Nunes, A. Pimentel, P. Barquinha, P. A. Carvalho, E. Fortunato and R. Martins, *J. Mater. Chem. C*, 2014, **2**, 6097–6103.

32 X. C. Jiang, T. Herricks and Y. N. Xia, *Nano Lett.*, 2002, **2**, 1333–1338.

33 P. Basnet and Y. Zhao, *J. Mater. Chem. A*, 2014, **2**, 911–914.

34 A. Wolcott, W. A. Smith, T. R. Kuykendall, Y. P. Zhao and J. Z. Zhang, *Small*, 2009, **5**, 104–111.

35 J. Steele and M. Brett, *J. Mater. Sci.: Mater. Electron.*, 2007, **18**, 367–379.

36 Y. He, P. Basnet, S. E. H. Murph and Y. Zhao, *ACS Appl. Mater. Interfaces*, 2013, **5**, 11818–11827.

37 W. Smith, A. Wolcott, R. C. Fitzmorris, J. Z. Zhang and Y. Zhao, *J. Mater. Chem.*, 2011, **21**, 10792–10800.

38 I. Hodgkinson, Q. H. Wu and J. Hazel, *Appl. Opt.*, 1998, **37**, 2653–2659.

39 R. N. Tait, T. Smy and M. J. Brett, *Thin Solid Films*, 1993, **226**, 196–201.

40 H. Zhu, W. Cao, G. K. Larsen, R. Toole and Y. Zhao, *J. Vac. Sci. Technol., B*, 2012, **30**, 030606.

41 C. Suryanarayana, *Prog. Mater. Sci.*, 2001, **46**, 1–184.

42 R. Köferstein, *J. Alloys Compd.*, 2014, **590**, 324–330.

43 J. Rodríguez-Carvajal, *Phys. B*, 1993, **192**, 55–69.

44 D. Channei, B. Inceesungvorn, N. Wetchakun, S. Ukritnukun, A. Nattestad, J. Chen and S. Phanichphant, *Sci. Rep.*, 2014, 4.

45 N. Wetchakun, S. Chaiwichain, B. Inceesungvorn, K. Pingmuang, S. Phanichphant, A. I. Minett and J. Chen, *ACS Appl. Mater. Interfaces*, 2012, **4**, 3718–3723.

46 R. Asahi, T. Morikawa, T. Ohwaki, K. Aoki and Y. Taga, *Science*, 2001, **293**, 269–271.

47 G. Ghadimkhani, N. R. de Tacconi, W. Chanmanee, C. Janaky and K. Rajeshwar, *Chem. Commun.*, 2013, **49**, 1297–1299.

48 S. J. A. Moniz, S. A. Shevlin, D. J. Martin, Z.-X. Guo and J. Tang, *Energy Environ. Sci.*, 2015, **8**, 731–759.

49 T. Hisatomi, J. Kubota and K. Domen, *Chem. Soc. Rev.*, 2014, **43**, 7520–7535.

50 A. Houas, H. Lachheb, M. Ksibi, E. Elaloui, C. Guillard and J. M. Herrmann, *Appl. Catal., B*, 2001, **31**, 145–157.

51 J. Jiang, K. Zhao, X. Xiao and L. Zhang, *J. Am. Chem. Soc.*, 2012, **134**, 4473–4476.

52 I. K. Konstantinou and T. A. Albanis, *Appl. Catal., B*, 2004, **49**, 1–14.

53 M. Neamtu, H. Siminiceanu, A. Yediler and A. Kettrup, *Dyes Pigm.*, 2002, **53**, 93–99.

54 A. Mills and J. S. Wang, *J. Photochem. Photobiol., A*, 1999, **127**, 123–134.

55 M. Aslam, I. M. I. Ismail, S. Chandrasekaran, H. A. Qari and A. Hameed, *Water, Air, Soil Pollut.*, 2015, 226.

56 S. Chen and L.-W. Wang, *Chem. Mater.*, 2012, **24**, 3659–3666.

57 L. Chen, S. Shet, H. Tang, H. Wang, T. Deutsch, Y. Yan, J. Turner and M. Al-Jassim, *J. Mater. Chem.*, 2010, **20**, 6962–6967.

58 J. W. Ager, M. R. Shaner, K. A. Walczak, I. D. Sharp and S. Ardo, *Energy Environ. Sci.*, 2015, **8**, 2811–2824.

59 M. E. A. Warwick, K. Kaunisto, D. Barreca, G. Carraro, A. Gasparotto, C. Maccato, E. Bontempi, C. Sada, T.-P. Ruoko, S. Turner and G. Van Tendeloo, *ACS Appl. Mater. Interfaces*, 2015, 7, 8667–8676.

60 L. Liao, Q. Zhang, Z. Su, Z. Zhao, Y. Wang, Y. Li, X. Lu, D. Wei, G. Feng, Q. Yu, X. Cai, J. Zhao, Z. Ren, H. Fang, F. Robles-Hernandez, S. Baldelli and J. Bao, *Nat. Nanotechnol.*, 2014, **9**, 69–73.

61 X. Yang, X. Lian, S. Liu, G. Wang, C. Jiang, J. Tian, J. Chen and R. Wang, *J. Phys. D: Appl. Phys.*, 2013, 46.

62 F. F. Abdi and R. van de Krol, *J. Phys. Chem. C*, 2012, **116**, 9398–9404.

63 Y. Pihosh, I. Turkevych, K. Mawatari, T. Asai, T. Hisatomi, J. Uemura, M. Tosa, K. Shimamura, J. Kubota, K. Domen and T. Kitamori, *Small*, 2014, **10**, 3692–3699.

64 H. Lachheb, E. Puzenat, A. Houas, M. Ksibi, E. Elaloui, C. Guillard and J. M. Herrmann, *Appl. Catal., B*, 2002, **39**, 75–90.